

# Integrating Point Sources to Map Anthropogenic Atmospheric Mercury Emissions in China, 1978–2021

Yuying Cui<sup>1,2</sup>, Qingru Wu<sup>1,2\*</sup>, Shuxiao Wang<sup>1,2</sup>, Kaiyun Liu<sup>3</sup>, Shengyue Li<sup>1,2</sup>, Zhezhe Shi<sup>1,2</sup>, Daiwei Ouyang<sup>1,2</sup>, Zhongyan Li<sup>4</sup>, Qinqin Chen<sup>1,2</sup>, Changwei Lü<sup>5,6</sup>, Fei Xie<sup>5,6</sup>, Yi Tang<sup>7</sup>, Yan Wang<sup>8</sup>, Jiming Hao<sup>1,2</sup>

<sup>1</sup>State Key Joint Laboratory of Environment Simulation and Pollution Control, School of Environment, Tsinghua University, Beijing 100084, China

<sup>2</sup>State Environmental Protection Key Laboratory of Sources and Control of Air Pollution Complex, Beijing 100084, China

<sup>3</sup>College of Environmental Science and Engineering, North China Electric Power University, Beijing, 102206, PR China

<sup>4</sup>Weiyang College, Tsinghua University, Beijing 100084, China

<sup>5</sup>School of Ecology and Environment, Inner Mongolia University, 010021, Hohhot, China

<sup>6</sup>Institute of Environmental Geology, Inner Mongolia University, 010021, Hohhot, China

<sup>7</sup>State Key Laboratory of Environmental Criteria and Risk Assessment, Chinese Research Academy of Environmental Sciences, 100012, Beijing, China

<sup>8</sup>College of Electromechanical Engineering, Qingdao University of Science and Technology, Qingdao 266061, China

16

Correspondence to: Qingru Wu (qrwu@tsinghua.edu.cn)

**Abstract.** Mercury emissions from human activities persist in the environment, posing risks to humans and ecosystem, and are regulated by the Minamata Convention. Understanding historical mercury emissions is critical for explaining its presence in the environment, and a long-term gridded emission inventory is essential for simulation and evaluation. While in recent previous years, some studies have improved looked at the historical trends of atmospheric emission inventory. The spatial resolution of emission inventories for recent years, have improved. However, limited inventories few have combined long time scales with high spatial resolution, which is essential for evaluating the legacy impacts of anthropogenic mercury emissions, particularly in regions with high levels of mercury emissions. Here we compile a new comprehensive point source database by fusing multiple data source, and integrate it with previous China Atmospheric Mercury Emission Model to develop a long-term gridded emission inventory for China, covering 1978-2021, named P-CAME. By integrating point source, P-CAME improves the accuracy of gridded emissions, reducing the normalized mean error by 108% compared to an inventory without point sources in the most recent year of 2021. The improved gridded emission data P-CAME highlights identifies potential pollutioned hotspots grids characterized by high cumulative emissions. It indicates revealing that 20% of cumulative emissions originate from just 0.3% of the grids, primarily distributed in Gansu, Yunnan, and Hunan Provinces. These areas are predominantly dominated by non-ferrous metal smelters or a mixed of emissions from sources including coal-fired industries and cement production. P-CAME also demonstrates consistency with observed Hg<sup>0</sup> (Gaseous elemental mercury) concentration trends over the past decade and shows potential to The improved gridded emissions inventory notably enhances the simulation of atmospheric mercury concentrations, particularly in urban areas, though its capacity is still limited by overall

35 model performance. ~~P-CAME inventory resulted in a 20-23% reduction in the normalized mean bias. The improved gridded~~  
36 ~~emission data identifies potential polluted grids characterized by high cumulative emissions. It indicates that 20% of~~  
37 ~~cumulative emissions originate from just 0.3% of the grids, primarily distributed in Gansu, Yunnan, and Hunan Provinces.~~  
38 ~~These areas are predominantly dominated by non-ferrous metal smelters or a mix of emissions sources including coal-fired~~  
39 ~~industries and cement production.~~ With ~~the~~ improvements in simulation accuracy spatial distribution accuracy and ~~the~~  
40 identification of highly polluted regions reliable long-term trend, this updated inventory ~~would greatly~~ will provide valuable  
41 data support for global emissions modelling, facilitate ~~the~~ assessments of mercury exposure recycling, and legacy impacts, and  
42 aid in effective management of cross-media mercury pollution the evaluation of Minamata Convention.

#### 43 **Keywords**

44 Speciated mercury; Emission inventory; Mercury concentration; GEOS-Chem; Cumulative emissions.

## 45 1 Introduction

46 Mercury is a persistent environmental pollutant that is harmful to the nervous systems and can affect health across generations.  
47 Human activities have liberated mercury from stable long-lived reservoirs, mainly geologic deposits and coal, to the Earth's  
48 surface, leading to 3-5 fold increase in mercury content in the land, atmosphere, and oceans since the industrial revolution  
49 (Streets et al., 2011; Corbitt et al., 2011; Selin, 2009; Selin et al., 2008). The increased load of mercury in the environment  
50 poses significantly risks to human health and ecosystem worldwide (Selin, 2009; Bishop et al., 2020; Amos et al., 2013; Li et  
51 al., 2022; Meng et al., 2011; Giang and Selin, 2016; Smith-Downey et al., 2010), promoting the establishment of the Minamata  
52 Convention on Mercury in 2013, a legally binding international treaty aimed at regulating mercury use and emissions in human  
53 activities. In accordance with the convention's regulation, the fifth Conference of the Parties had formally initiated the first  
54 effectiveness evaluation of the Convention at the end of 2023. Updated historical mercury emissions, with both temporal  
55 continuity and spatial precision, are critical and urgent to understand the changing trajectory and present state of mercury  
56 pollution and to evaluate the effectiveness of pollution control efforts.

57 Amidst a wide array of studies, ~~three-four~~ main global emission inventories stand out for their comprehensiveness and broadly  
58 implication in CTMs (Chemical transport models): those established by Streets (Streets et al., 2011; Streets et al., 2019),  
59 EDGAR (Muntean et al., 2018; Muntean et al., 2014), ~~and~~ AMAP/UNEP (AMAP/UNEP, 2013, 2019), and WHET (Zhang et  
60 al., 2016b). The annual emission magnitudes across inventories are ranked as WHET > Streets > AMAP/UNEP > EDGAR.  
61 Spatially, higher-emission grids are observed in WHET, Streets, and AMAP/UNEP for 2010, whereas EDGAR shows lower  
62 emissions, particularly in East and South Asia. Regarding long-term trends, EDGAR and Streets exhibit a gradual increase in  
63 emissions from 1980–2012 and 1980–2015, respectively. In contrast, WHET shows a decline followed by an increase during  
64 1990–2010. These emission inventories have been extensively used in CTMs to simulate the atmospheric transport,  
65 transformation, and deposition of Hg. Comparing simulated Hg<sup>0</sup> concentrations with observations provides a critical metric  
66 for evaluating the performance of emission inventories in CTMs. Despite discrepancies among inventories in terms of emission  
67 magnitudes, species composition, and spatial distributions, a study employing the ECHMERIT model (Jung et al., 2009)  
68 reported no statistically significant differences in regression slopes when inventory-based simulations were compared with  
69 observational data (Simone et al., 2016). In terms of trends, both Streets and EDGAR indicate increasing emissions. However,  
70 when Streets inventory data were used as CTMs input, the simulated Hg<sup>0</sup> concentrations conflicted with the observed decline  
71 in atmospheric Hg<sup>0</sup> concentrations in the Northern Hemisphere during 2005–2020 (Feinberg et al., 2024). Anthropogenic  
72 emissions were identified as the primary driver of the divergence between simulated and observed Hg<sup>0</sup> concentrations and the  
73 associated declining trend (Feinberg et al., 2024). The WHET inventory, which incorporates updated country-specific  
74 emissions for China, India, the U.S., and Western Europe, successfully reproduced observed atmospheric Hg concentration  
75 declines in GEOS-Chem simulations (Zhang et al., 2016b). Emission estimates from WHET for 1990, 2000, and 2010 were

76 1.3 to 2.4 times higher than those reported by Streets or EDGAR, highlighting the pivotal role of regional emissions in  
77 accurately capturing global emission trends and aligning them with observational data.

78 Particularly, China has garnered great attention due to its substantial emission levels, complex source profiles, and swift  
79 advancement of control technologies. These factors collectively pose challenges to precisely estimate atmospheric mercury  
80 emissions in China. Prior researches have reduced the uncertainty of emission factors through extensive field experiments in  
81 China, culminating in the development of regional, sectoral, and national emission inventories in specific years (Wu et al.,  
82 2006; Tian et al., 2010; Tian et al., 2015; Zhang et al., 2015; Zhao et al., 2015; Wu et al., 2016; Liu et al., 2019; Zhang et al.,  
83 2023). Among these, three notable decadal emission inventories have been developed (Tian et al., 2015; Wu et al., 2016; Zhang  
84 et al., 2023). Yet, variations in emission trends, particularly after 2010, were pronounced. Tian et al., (2015) neither provided  
85 long-term spatial characteristics nor species profiles, limiting the comprehensiveness of their inventory. Wu et al., (2016)  
86 presented gridded emission data, but its reliance on population and GDP proxies introduced a notable degree of uncertainty  
87 regarding spatial accuracy. Zhang et al., (2023) took a step forward by aligning emissions from several critical sectors with  
88 point-source locations; however, detailed gridded emissions were made available only for 2010, 2015, and 2020. These  
89 inventories underscore a persistent gap in fine-resolution gridded and speciated mercury emission data in China, which is  
90 essential for evaluating the present state of mercury pollution and supporting effective regulatory actions.

91 Here we introduce a novel, speciated annual mercury emission inventories spanning from 1978 to 2021, derived from the  
92 Point-source Integrated China Atmospheric Mercury Emission Model, herein referred to as P-CAME inventories. This updated  
93 inventory opens avenues for enhancing our comprehension of atmospheric mercury pollution. Crucially, our inventory's  
94 accurate, annual, high-resolution emission maps can identify cumulative emission hotspots, and highlight areas of potential  
95 multi-media environmental impacts. This inventory is publicly accessible and maintains temporal and spatial consistency with  
96 detailed information; therefore, it can contribute to improving Hg simulation performance in future studies and lays a solid  
97 foundation for discussions on anthropogenic emissions, atmospheric pollution and health implications. Furthermore, it is  
98 poised to offer robust support for the inaugural evaluation of the effectiveness of the Minamata Convention.

## 99 **2 Methods**

### 100 **2.1 P-CAME Emission inventory**

101 This study coupled the China Atmospheric Mercury Emission Model (Zhang et al., 2015; Wu et al., 2016) with the point source  
102 database to generate the P-CAME emission inventory. The studied 24 sectors (Table S1) were divided into 3 categories (Tier  
103 1-3). Tier 1 was the point source emission category, including coal-fired power plants (CFPP), zinc smelting (Zn), leading  
104 smelting (Pb), copper smelting (Cu), cement production (CEM), iron and steel production (ISP), coal-fired industrial boilers  
105 (CFIB), municipal solid waste incineration (MSWI), large scale golden production (LSGP). Emissions in Tier1 were computed

106 using facility-level activity and dynamic technology-based emission factors (Equation S1). Emissions from other sectors were  
107 calculated using provincial activity data combined with probabilistic technology-based emission factors (Tier2, Equation S2)  
108 or time-varying emission factors (Tier3, Equation S3). To acquire gridded emissions for sectors in Tier 2 and Tier 3, source-  
109 specific spatial proxies (Table S1) were used to allocate provincial area sources to grids at a resolution of  $0.25^{\circ} \times 0.3125^{\circ}$ .  
110 Emissions from each point source were assigned to the grid corresponding to their geographical coordinates and combined  
111 with nonpoint source data to create comprehensive emission maps at a resolution of  $0.25^{\circ} \times 0.3125^{\circ}$  for total mercury ( $\text{Hg}^{\text{T}}$ )  
112 and each mercury species, namely gaseous elemental mercury ( $\text{Hg}^0$ ), gaseous oxidized mercury ( $\text{Hg}^{\text{II}}$ ), and particulate-bound  
113 mercury ( $\text{Hg}_{\text{p}}$ ). ~~The new inventories, encompassing speciated mercury emissions from point sources, nonpoint sources, were~~  
114 ~~named as P-CAME. Annual emission inventories for each mercury species during 1978-2021 are available.~~

### 115 **2.1.1 Point source emission model (Tier 1)**

116 Annual facility-level activity was from point source database. Point source database combined point sources we could get from  
117 Environmental Statistics, Industry Associations, Pollution Source Censuses, yearbooks of various industry sectors and  
118 previous studies, as shown in Table S2. To construct the point source database, detailed data collected for each facility included  
119 corporate name, type of industry, capacity, types of raw materials or fuels, production or consumption levels, production or  
120 combustion processes, control technologies, and geographical information. Data from various sources were integrated based  
121 on the Unified Corporate Social Credit Code unique to each enterprise. Missing information of point sources in the database  
122 were addressed using data retrieval or assimilation methods. The Baidu Map System (<http://jingweidu.757dy.com/>) and  
123 Qichacha website (<https://www.qcc.com/>) were used to fill in missing coordinates and operational years, respectively. For  
124 2013-2021, we acquired point sources activity for each year and validated and adjusted the activity by comparing it with  
125 provincial activity from the yearbook. For earlier years, where varying activity were more difficult to obtain, we used point  
126 source data from the best-validated year and time-varying provincial activity to estimate point source activity for the period  
127 1978-2012. Specifically, for the annual activity, we first extracted data of operating facilities in the current year based on their  
128 operational years. Then, the activity was obtained by multiplying the provincial activity in that year by the proportion of the  
129 point source activity in the province. Dynamic technology-based emission factors for point sources were derived from  
130 provincial mercury concentrations in fuel or raw materials, combustion or production technology release rates, air pollution  
131 control device (APCDs) removal efficiencies, and speciation profiles (Equation S1). Raw mercury concentrations in fuel or  
132 raw materials were obtained from our previous studies (Zhang et al., 2012; Wu et al., 2012; Liu et al., 2018). Release rates and  
133 mercury removal efficiency were from field experiments (Zhang et al., 2016a; Zhang, 2012; Chang and Ghorishi, 2003; Omine  
134 et al., 2012). The removal efficiencies and speciation profiles for APCDs were detailed in Table S3.

### 135 2.1.2 Probabilistic technology-based emission model (Tier 2)

136 Annual provincial activity for sectors in Tier 2 were obtained from statistical yearbooks (Table S2). To estimate mercury  
137 emissions with greater accuracy and reduced bias, Monte Carlo simulations were applied to produce probabilistic technology-  
138 based emission factors, addressing the variability and uncertainty in key parameters. Emission factors were calculated based  
139 on the provincial mercury concentration in fuel or raw materials (log-normal distribution), release rates associated with  
140 combustion or production technologies (as specified for coal-fired sectors), removal efficiencies of APCDs (normal or Weibull  
141 distributions), and the proportions of mercury species determined by APCDs combinations (Equation S2). Raw mercury  
142 concentration data and their standard deviations were sourced from previous studies (Zhang et al., 2012; Wu et al., 2012; Liu  
143 et al., 2018; Liu et al., 2019), while mercury removal efficiencies and release rates were obtained from prior research based on  
144 field experiments (Zhang et al., 2016a; Zhang, 2012; Chang and Ghorishi, 2003; Omine et al., 2012). Speciated mercury  
145 proportions for various APCD combinations were derived from our earlier work (Liu et al., 2019; Zhang et al., 2023; Wu et  
146 al., 2016). By incorporating these parameters into Monte Carlo simulations, probabilistic emission factors were generated,  
147 providing a robust and comprehensive estimation of mercury emissions across Tier 2 sectors.

### 148 2.1.3 Time-varying emission model (Tier 3)

149 Annual provincial activity for sectors in Tier 3 were obtained from statistical yearbooks, Chinese environmental statistics, and  
150 investigation reports (Table S2). The emission factors for Tier 3 sectors dynamically changed with technology iterations,  
151 assuming that emission factors fit a transformed normal distribution due to the dynamics of technology change (Tian et al.,  
152 2015; Streets et al., 2011). The emission factor for a specific year was calculated using the emission factor at the beginning  
153 year of technology transition ( $ef_a$ ) and the best achievable emission factor ( $ef_b$ ), as outlined in Equation S3. The parameters  $ef_a$ ,  
154  $ef_b$ , and the curve shape parameter  $S$  were derived from previous studies (Tian et al., 2015; Streets et al., 2011; Wu et al., 2016;  
155 Wu et al., 2006; Zhang et al., 2015).

156 Provincial emissions from sectors in Tier 2 and Tier 3 were allocated to grids at a resolution of  $0.25^\circ \times 0.3125^\circ$  using a newly  
157 developed spatial allocation system, as detailed in Table S1. This allocation relied on proxies such as GDP, population data,  
158 and a roadmap dataset. Provincial non-point sources were first allocated to the city level based on GDP and then further  
159 distributed to the grid level using either population or road network datasets, as specified in Equation S4. City-level GDP data  
160 were extracted from statistical yearbooks, with the GDPs of primary, secondary, and tertiary industries utilized for various  
161 sectors, as detailed in Table S1. Population data at the grid level were obtained from the resource and environmental science  
162 data registration and publication system (Xu, 2017). While population data were available for select years (1990, 1995, 2000,  
163 2005, 2010, 2015, and 2019), data for intermediate years were interpolated. Specifically, data for the years 1978-1989 were  
164 estimated based on available data and observed trends during the period of 1990-2000. Road network data utilized in this study  
165 were sourced from OpenStreetMap (<https://www.openstreetmap.org/>). The widths of various route types in the road network

166 were determined based on classifications provided in the Interim Provisions on Urban Planning Quota Index (MOHURD,  
167 1980). These routes were then converted into areas and subdivided into grids. The gridded routes served as a proxy for the  
168 spatial distribution of atmospheric mercury emissions from the transportation sector. To develop this long-term anthropogenic  
169 mercury emission dataset, software tools such as ArcGIS and Matlab were employed.

## 170 2.2 Uncertainty analysis

171 Monte Carlo simulation assessed mercury emission uncertainty using key parameters and their probability distributions.  
172 Parameters included activities, mercury concentrations in fuel/raw materials, and mercury removal efficiencies of APCDs.  
173 Activities were normally distributed with variation coefficients of 5%-30% (Liu et al., 2019). Mercury concentrations followed  
174 a log-normal distribution and mercury removal efficiencies followed normal or Weibull distributions, which were generated  
175 based on field experiments (Zhang et al., 2012; Wu et al., 2012; Liu et al., 2018; Zhang et al., 2016a; Zhang, 2012; Chang and  
176 Ghorishi, 2003; Omine et al., 2012). MATLAB conducted 10,000 Monte Carlo simulations. Mean values served as best  
177 estimates, with 2.5% and 97.5% quantiles establishing lower and upper limits of simulation results.

## 178 ~~2.3 Simulation and validation comparison~~ Evaluation and validation of emission inventory

179 We applied a global 3-D atmospheric chemistry model (GEOS-Chem, v12.6.3, <http://geos-chem.org>) to simulate atmospheric  
180 mercury concentrations from 2006 to 2021. A three-year spin-up (2006-2008) was used to achieve balanced concentrations,  
181 which serve as the restart field for analysis year (2009-2021). The global simulation was conducted at a resolution of  $2.0^{\circ} \times$   
182  $2.5^{\circ}$  to provide boundary conditions for a nested simulation over the China region, which had a finer at a resolution of  
183  $0.25^{\circ} \times 0.63425^{\circ}$  and 47 vertical levels. Meteorological input data were driven by the Modern-Era Retrospective analysis  
184 for Research and Applications, Version 2 (GEOS-FPMERRA2) (Gelaro et al., 2017). For the global simulation, the EDGAR  
185 emission inventory was used as it provides long-term emissions data for the entire simulation period. However, since EDGAR  
186 tends to underestimate emissions in China, we replaced China's emission with the P-CAME inventory. Biomass burning  
187 emissions were calculated based on GFED4 (van der Werf et al., 2017), while geogenic activities, soil emission and re-emission  
188 followed the calculation scheme outlined in Selin et al., (2008). The chemical scheme in v12.6.3 involves the oxidation of  $\text{Hg}^0$   
189 through a two-step mechanism initiated by Br. Photoreduction of  $\text{Hg}^{2+}$  occurs in the aqueous phase and is governed by the  $\text{NO}_2$   
190 photolysis rate and organic aerosol concentrations (Horowitz et al., 2017).

191 To assess the impacts of the point source inventory, we designed two simulation scenarios with different anthropogenic  
192 emissions inputs: one using P-CAME and the other relying solely on proxies for emission allocation, referred to as "only  
193 proxy-based" thereafter. In the only proxy-based inventory, original point source sectors were initially calculated at the  
194 provincial level and then distributed to grids based on secondary GDP and population. We compared the simulations from  
195 both scenarios with monthly observations of atmospheric mercury concentrations at 2020. For the long-term simulation, we  
196 evaluated and compared the results using P-CAME against observed data to assess its performance over time. We applied



197 Normalized Mean Bias (NMB), Normalized Mean Error (NME), Root Mean Square Error (RMSE), and Pearson Correlation  
198 Coefficient (R) to quantify these comparisons, with their calculation equations provided in Equations S5–S8.  
199 We included Hg<sup>0</sup> concentration observations from 10 sites, comprising 4 urban sites and 6 rural sites (Sun et al., 2024; Wu et  
200 al., 2023; Shao et al., 2022; Feng et al., 2024; Tang et al., 2018). For the Chongming, Tsinghua, Miyun, and Hohhot sites, we  
201 present long-term observational data for the first time from our own measurements at these locations. Most sites, except for  
202 Qingdao, have long-term observations, enabling a comparison of long-term trends with simulations. At the Qingdao site, data  
203 are only available for 2020–2021; thus, this dataset was used exclusively to compare simulations based on the P-CAME and  
204 only proxy-based inventories. Additionally, observed meteorological data were obtained from NOAA’s National Climatic  
205 Data Center (NCDC).

206 **3 Results and discussions**

207 **3.1 Spatial distribution pattern of atmospheric mercury emissions**

208 This study developed an extensive point source database covering the period from 1978 to 2021. For instance, in the most  
209 recent year of 2021, the inventory includes over 26,000 industrial facilities. Atmospheric mercury emissions in 2021 were  
210 estimated to be 358–351 t, with Hg<sup>0</sup>, Hg<sup>II</sup>, and Hg<sub>P</sub> accounting for 5554%, 4344%, and 2%, respectively. The point source  
211 emissions accounted for over 85% in 2021. The point sources were unevenly distributed, primarily concentrated in East and  
212 South China (Fig. 1). Their emissions exhibited a broad spectrum of orders of magnitude, with 90% of the total emissions  
213 budget being dominated by only the top one third large point sources (Fig. 1). Among the top one third large point sources,  
214 68% were cement production (CEM) facilities, widely distributed in North China, East China, South China, Central China and  
215 Southwest China as indicated by P-CAME.

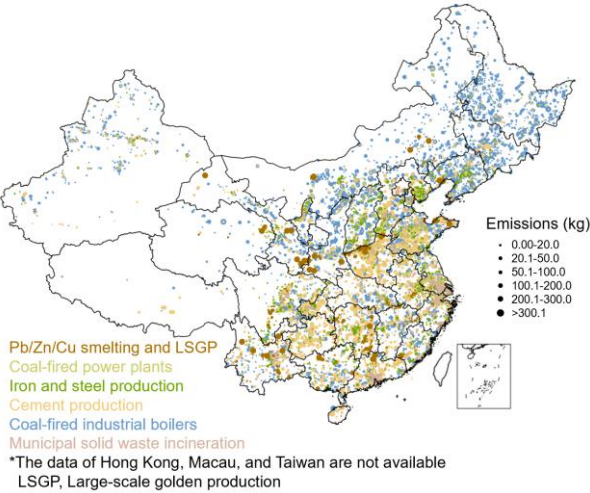




**Figure 1 Spatial distribution of point source emissions at 2021.**

The integration of point sources in the P-CAME inventories improved the accuracy of the located gridded emissions, compared to the only proxy-based inventory (Fig. 2a & b). To quantify these differences, ~~the normalized mean bias (NMB, Equation S1)~~ and ~~the normalized mean error (NME, Equation S2)~~ were employed. The calculated NMB and NME for all grids stood at 1% and 108%, respectively. The low NMB alongside the high NME indicated a pronounced discrepancy between P-CAME inventories and the only proxy-based inventory, primarily due to misalignment in grids with high and low emissions. Overall, proxy method tended to overestimate emissions in densely populated areas, notably in capital cities such as Lanzhou, Xi'an, Kunming, Guizhou and Guangdong, while significantly underestimated emissions in industrial clusters like Jiaozuo, Baoji, Handan, Tangshan and Chenzhou (Fig. 2c). At a more granular grid scale, discrepancies included both overestimations and underestimations. For example, in Handan's grids, emissions using proxy method were overestimated in the eastern parts and underestimated in the west, contributing to the substantial NME value (108%). This illustrated that the emission using the proxy method inaccurately distributed emissions not just between cities but also within individual city grids, causing significant variations.

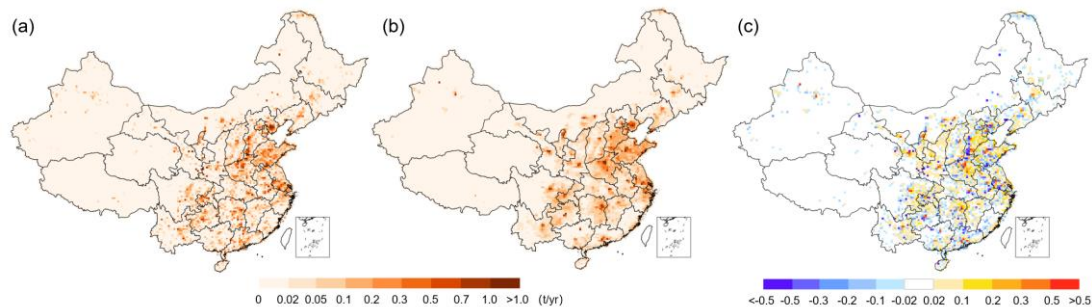


**Figure 2 Comparison of spatial distribution between (a) P-CAME and (b) the only proxy-based inventory; (c) absolute difference of these two distributions.**

### 3.2 Temporal trends of annual emissions

The analysis of long-term point source emissions enabled a reassessment of historical mercury emission trends and sector contributions from 1978 to 2021. The overall trend showcased an initial rise in emissions, peaking in 581 t, following which the emissions declined. This trend reflected substantial shifts across key sectors such as coal-fired power plants (CFPP), non-ferrous metal smelting (NFMS), cement production (CEM), and coal-fired industrial boilers (CFIB) (Fig. 3a). By 1990, emissions nearly doubled from 1978, reaching 272 t, with an average annual rising rate of 5% and CFIB, NFMS, and CFPP being the primary sources. The NFMS emissions peaked in 2004, following which the emissions declined, while the CEM emissions rose faster, and CEM becoming the second-largest contributor by 2010. The decade ending in 2010 saw emissions reaching 558 t, with an average growth rate of 4%, despite a brief period of reduction due to drops in the CFPP and NFMS

emissions. The following decade highlighted a general decline in emissions from NFMS, CFIB, and CFPP, but the CEM emissions were still increasing, making it the largest contributor to the total emissions since 2011. It was until 2021 that a slight increase in total emissions was noted, driven mainly by rises in municipal solid waste incineration (MSWI) and the CEM emissions.

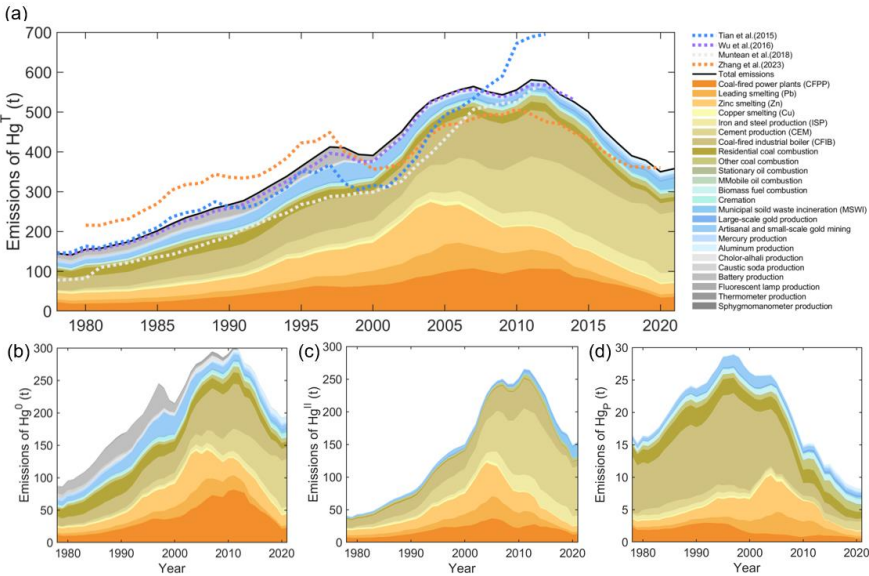


**Figure 3 Annual anthropogenic mercury emissions and comparison with other emission inventories. (a) Hg<sup>T</sup>; (b) Hg<sup>0</sup>; (c) Hg<sup>II</sup>; (d) Hg<sub>P</sub>.**

In line with the trend observed in total mercury emissions, annual speciated mercury emissions also followed a pattern of initial increase followed by a decline. Specifically, annual Hg<sup>0</sup> emissions rose from 89 t to 299 t during the period of 1978-2011, subsequently decreasing to 188 t by 2021 (Fig. 3b). Notably, three peaks occurred during the increasing phase of Hg<sup>0</sup> emissions: the first peak in 1997 due to battery production emissions, the second peak in 2007 resulting from reduced activity levels and enhanced SO<sub>2</sub> control in CFPP, and the third peak in 2011 due to enhanced NO<sub>x</sub> control in CFPP. Annual Hg<sup>II</sup> emissions increased from 42 t to 267 t during 1978-2011, followed by a decline to 155 t by 2021 (Fig. 3c). During the increasing phase of Hg<sup>II</sup> emissions, two peaks occurred: the first peak in 2007 was attributed to a rapid decline in NFMS and CFPP emissions during 2007-2009, while the second peak in 2011 was caused by a peak in continuous CEM emissions. Annual Hg<sub>P</sub> emissions rose from 17 t to 29 t during 1978-1997, then decreased to 8 t by 2021 (Fig. 3d), with the peak occurring in 1997 mainly dominated by emissions in CFIB.

Overall, mercury emissions in China have experienced three distinct phases: an increase from 1978 to 2007, stabilization from 2008 to 2012, and a decrease from 2013 onwards. These phases reflect varying emission and control characteristics. The first phase (1978-2007) was marked by rapid growth in activity levels, leading to a significant increase and peak in emissions. The

262 second phase (2008-2012) saw the combined effects of continued growth in activity levels and the implementation of emission  
263 controls, resulting in relatively stable changes. The third phase (2013-2021) was characterized by a reduction in emissions  
264 driven by more stringent emission controls. These three phases were also clearly delineated in the patterns of gridded emissions  
265 depicted across three rows in Fig. S1. During the first period, there was an average 5% increase in annual emissions,  
266 particularly noticeable in the border areas of North China, Central China, and the Yangtze River Delta (first row of Fig. S1).  
267 Throughout the second period (2008-2012), the emissions remained relatively unchanged, with an average 0.5% increase in  
268 annual emissions (second row of Fig. S1). In the subsequent third period (2013-2021), a noticeable reduction with an average  
269 5% decrease in annual emissions was observed, particularly in area increased during the growth period (third row of Fig. S1).

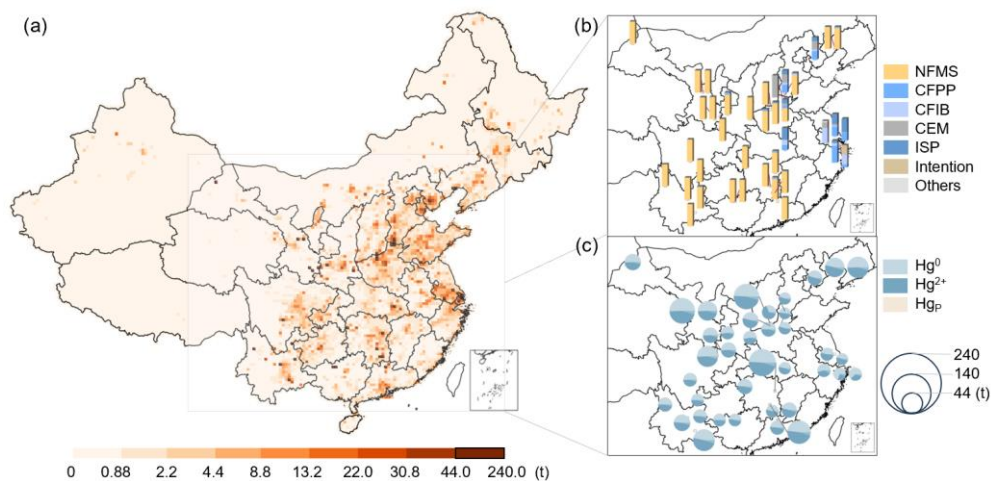
### 270 3.3 Comparison with previous emissions inventories

271 The P-CAME emission inventory was evaluated against prior long-term inventories in China, demonstrating good alignment  
272 with our earlier findings reported by Wu et al., (2016) and closely matching the estimates by Tian et al., (2015) until 1995 (Fig.  
273 3a). A detailed sectoral comparison (Fig. S2) revealed that the congruence with Tian et al., (2015) was somewhat coincidental.  
274 This study reported lower emissions from the NFMS and intentional mercury use, but higher emissions from mercury  
275 production than Tian et al., (2015) before 1995. Post-1995, the primary discrepancies with prior studies stemmed from the  
276 zinc, lead, copper sectors, and the CFPP. Differences with the Zhang et al., (2023) study was in two periods—before and after  
277 1998—based on total mercury emissions (Fig. 3a). Before 1998, our study reported lower emissions, mainly attributed to a  
278 reduced estimate from the CFIB by approximately 40 t. A higher reported utilization of air pollution control devices (APCDs)  
279 accounted for the underestimation. After 1998, our study reported higher emissions, particularly in the CEM and NFMS sectors,  
280 attributed to differences in mercury concentration in fuels or raw materials and the application of APCDs. The uncertainty  
281 range, defined by the 2.5% and 97.5% quantiles, represents a 95% confidence interval, indicating a 95% probability that the  
282 true value lies within this range. For P-CAME emission inventory, the uncertainty range was subjected to (-16.1%, to -15.9%)  
283 in 2021, reflecting lower uncertainty in the parameters. In 1978, the uncertainty range was but reached (-21.8%, % to 21.5%) %.  
284 primarily due to greater uncertainty in the in 1978 due to the higher uncertainty of parameters after resulting from data fusion  
285 (Fig. S3). The uncertainty ranges were among the lowest reported in existing studies (Wu et al., 2016; Liu et al., 2019; Zhang  
286 et al., 2023).

### 288 ~~4.2.3.4 Identifying cumulative emission hotspots~~ Identification of cumulative emission hotspots

289 Atmospheric mercury emissions can affect human health through air inhalation; however, their deposition on surfaces and  
290 prolonged retention pose even greater risks by causing cross-media impacts and persistent threats. The continuous, high-  
291 resolution, and spatially detailed P-CAME inventories enable the identification of hotspots for cumulative atmospheric  
292 mercury emissions since 1978, marking the start of China's economic expansion with its reform and opening-up policy. Over

293 this period, total mercury emissions reached 16,537 t, with  $\text{Hg}^0$  accounting for 9,093 tons (55.0%),  $\text{Hg}^{\text{II}}$  for 6,570 t (39.7%),  
294 and  $\text{Hg}_\text{p}$  for 874 t (5.3%). The cumulative emissions map, as depicted in Fig. S4a, identifies critical hotspots that, despite  
295 covering only 0.3% of the grids, contributed to 20% of the total emissions. These hotspots, where cumulative emissions  
296 exceeded 44 t (averaging more than 1 t annually), were chiefly found in Gansu, Yunnan, and Hunan Provinces. Emission  
297 sources within these hotspots fall into two primary categories based on sectoral contributions: those predominantly influenced  
298 by NFMS and those influenced by sectors other than NFMS, as shown in Fig. S4b. Grids dominated by NFMS represented  
299 76% of the areas with high cumulative emissions, where NFMS's contributions averaged 96%. These areas also exhibited a  
300 significant presence of  $\text{Hg}^{\text{II}}$  and  $\text{Hg}_\text{p}$ , averaging 51%, as indicated in Fig. S4c. Conversely, grids primarily affected by other  
301 sectors—such as CFPP, CFIB, CEM, Iron and steel production (ISP)—were located in Hebei, Henan, Hubei, Jiangsu, and  
302 Shanghai. The sectoral contribution to the hotspots of cumulative emissions indicated that grids with NFMS tends to cause  
303 severe cross-media mercury pollution due to their high emission intensity and  $\text{Hg}^{\text{II}}$  proportion.



304  
305 **Figure S4 Spatial distribution of cumulative mercury emissions. (a) Total mercury emissions; (b) Sectors contribution for total**  
306 **mercury emissions in hotspots; (c) Speciation profiles in hotspots.**

307 To further inform future pollution control strategies, we analyzed the atmospheric mercury emission hotspots for 2021, defined  
308 by emissions exceeding 1 t. Remarkably, half of the hotspots identified in 2021 coincided with those identified through  
309 cumulative emission analyses (Fig. S45). These overlapping hotspots were predominantly found in Gansu, Shaanxi, Henan,  
310 and Hebei provinces. In detail, Gansu and Shaanxi's hotspots were mainly attributed to emissions from NFMS, whereas Henan  
311 and Hebei's hotspots were largely due to emissions from the CEM. These areas warrant heightened focus, as addressing  
312 pollution here involved not only mitigating the impact of historical emissions but also urgently implementing controls on  
313 current emissions to prevent further environmental degradation. Moreover, new hotspots emerging in 2021 that did not  
314 coincide with historical cumulative emission hotspots were primarily located in Hebei, Henan, and Anhui Provinces (Fig. S45),

315 with CEM emissions contributing an average of 82% to these areas. While grids in Yunnan, Hunan, and Guangxi Provinces  
316 had high cumulative emissions, their 2021 emissions did not reach similar levels. Therefore, it is clear that future efforts in  
317 pollution prevention and control should prioritize areas with both significant cumulative emissions and high recent emissions,  
318 especially those impacted predominantly by cement industry activities. This focused approach is essential to simultaneously  
319 tackle the challenges of accumulated historical pollution and prevent the exacerbation of current emission levels, ensuring  
320 targeted and effective pollution control measures.

## 321 **4 Discussions**

### 322 **4.13.5 Impacts on the simulation of atmospheric mercury concentrations**Long-term simulation of atmospheric mercury 323 concentrations

324 The temporal and spatial distributions of annual atmospheric Hg<sup>0</sup> concentration are presented in Fig. 5. During 2011 to 2021,  
325 the simulated Hg<sup>0</sup> concentrations showed a declining trend, with the maximum values decreasing from 5.7 ng/m<sup>3</sup> to 3.0 ng/m<sup>3</sup>,  
326 and the national average dropping slightly from 1.5 ng/m<sup>3</sup> to 1.4 ng/m<sup>3</sup>. The spatial distribution analysis (Fig. 5) highlights a  
327 decline of simulated Hg<sup>0</sup> concentration in high-emission regions. However, the simulated magnitude of decline fails to capture  
328 the observed decline at monitoring sites, primarily due to an underestimation of Hg<sup>0</sup> concentration from 2010-2013, when  
329 anthropogenic emissions peaked in China (Fig. S5). This issue has also been existed in previous studies, which found that  
330 GEOS-Chem simulations underestimate Hg<sup>0</sup> concentration during this period (Liu et al., 2019; Sun et al., 2024). The  
331 underestimation may stem from either the model or our anthropogenic emission inventory. Observational studies have shown  
332 that the decline in anthropogenic emissions is the key driver behind the decrease in Hg<sup>0</sup> concentrations at both background  
333 sites (Changbai, Ailao, Damei, Waliguan, Chongming) (Feng et al., 2024; Tang et al., 2018), and urban sites (Nanjing) (Sun  
334 et al., 2024). To explore reasons for simulation underestimation, we compared the decline rates of observed Hg<sup>0</sup> concentration,  
335 simulated Hg<sup>0</sup> concentration and anthropogenic emissions at these sites, as shown in Table 1. For each site, the decline rate of  
336 observed Hg<sup>0</sup> concentration was calculated as the difference between maximum value and the concentration at the end of  
337 observation period, divided by the maximum value (see Equation S9 for an example calculating at Changbai). The same  
338 method was applied to calculate decline rates for simulated Hg<sup>0</sup> concentration, national total Hg<sup>0</sup> emissions, Hg<sup>0</sup> emissions  
339 from the 9 surrounding grids (approximately 500 km × 500 km), and Hg<sup>0</sup> emissions from the current grid over the same  
340 period.

341 As shown in Table 1, the decline rates of observed Hg<sup>0</sup> concentrations vary across different site types based on their location  
342 and emission impacts: (1) Background sites (Changbai, Ailao, Damei, Waliguan): These high-altitude sites with minimal local  
343 emissions represent national even global impacts. Their observed Hg<sup>0</sup> concentration decline rates closely align with the national  
344 total Hg<sup>0</sup> emission decline rates and are significantly higher than simulated Hg<sup>0</sup> concentration decline rates. (2) Regional  
345 background sites (Chongming, Miyun): Located in suburban areas, these sites reflect regional impacts. Their observed Hg<sup>0</sup>

concentration decline rates align more closely with the emission decline rates from nearby grids (9 surrounding grids) and are also much higher than simulated  $\text{Hg}^0$  decline rates. (3) Urban sites (Nanjing, Tsinghua, Hohhot): Urban sites are influenced by diverse emission sources, making it difficult to directly associate observed  $\text{Hg}^0$  concentrations with specific emission types. At Nanjing site, impacted by point source emissions from CFPP and CEM within the local grid, the observed decline rates closely align with local emission decline rates and are higher than simulated rates. At Tsinghua site, impacted by transported emissions from adjacent provinces, the observed  $\text{Hg}^0$  decline rates are comparable to the national total  $\text{Hg}^0$  emission decline rates. At Hohhot site, situated at a high altitude and impacted by broader area emissions, the observed  $\text{Hg}^0$  decline rates align with national total  $\text{Hg}^0$  emission decline rates.

The observed decline rate matches the emission decline rate and exceeds the simulated rate at all sites. This suggests that our anthropogenic emissions inventory is reasonable and should have reproduced the observed trends. Potential reasons for the model's underestimation include: (1) Boundary conditions. Boundary conditions play a critical role in determining the global background concentration of  $\text{Hg}^0$  in nested simulations. However, global anthropogenic emissions used in simulations often fail to capture the observed decline trend in  $\text{Hg}^0$  concentrations. For example, observations from the Northern Hemisphere indicate a decline of approximately  $0.011 \text{ ng m}^{-3} \text{ yr}^{-1}$ , while simulations show only a slight decline of  $0.0014 \text{ ng m}^{-3} \text{ yr}^{-1}$  (Feinberg et al., 2024). This discrepancy introduces bias in nested simulation trends, particularly at background sites. The inability of boundary conditions to reflect observed trends highlights a key limitation in current simulation. (2) Legacy re-emissions. Legacy re-emissions refer to the re-emission of previously deposited Hg. These  $\text{Hg}^0$  emissions diffuse back into the atmosphere and are reported to contribute significantly to current atmospheric mercury concentration (Angot et al., 2021) or deposition (Amos et al., 2013). For example, studies suggest that legacy re-emissions account for approximately 60% of atmospheric deposition, compared to 27% from anthropogenic emissions (Amos et al., 2013). (3) Transport process and wind field. Transport process plays a critical role in controlling  $\text{Hg}^0$  concentrations and trends (Roy et al., 2023), with wind field being a key factor in determining transport process (Brasseur and Jacob, 2017; Yang et al., 2024). By comparing simulated 10 m wind speed from MERRA2 with observed wind speed, we found discrepancies in the monthly wind speed trends between MERRA2 and meteorological observations (Fig. S6). These inconsistencies in monthly trends suggest a potential bias in MERRA2 wind speed data, consistent with findings from other evaluation studies (Miao et al., 2020). Similar biases are observed in wind direction when comparing MERRA2 with observations (Fig. S7). These biases likely contribute to transport simulation errors and may significantly underestimate  $\text{Hg}^0$  concentrations in the model.



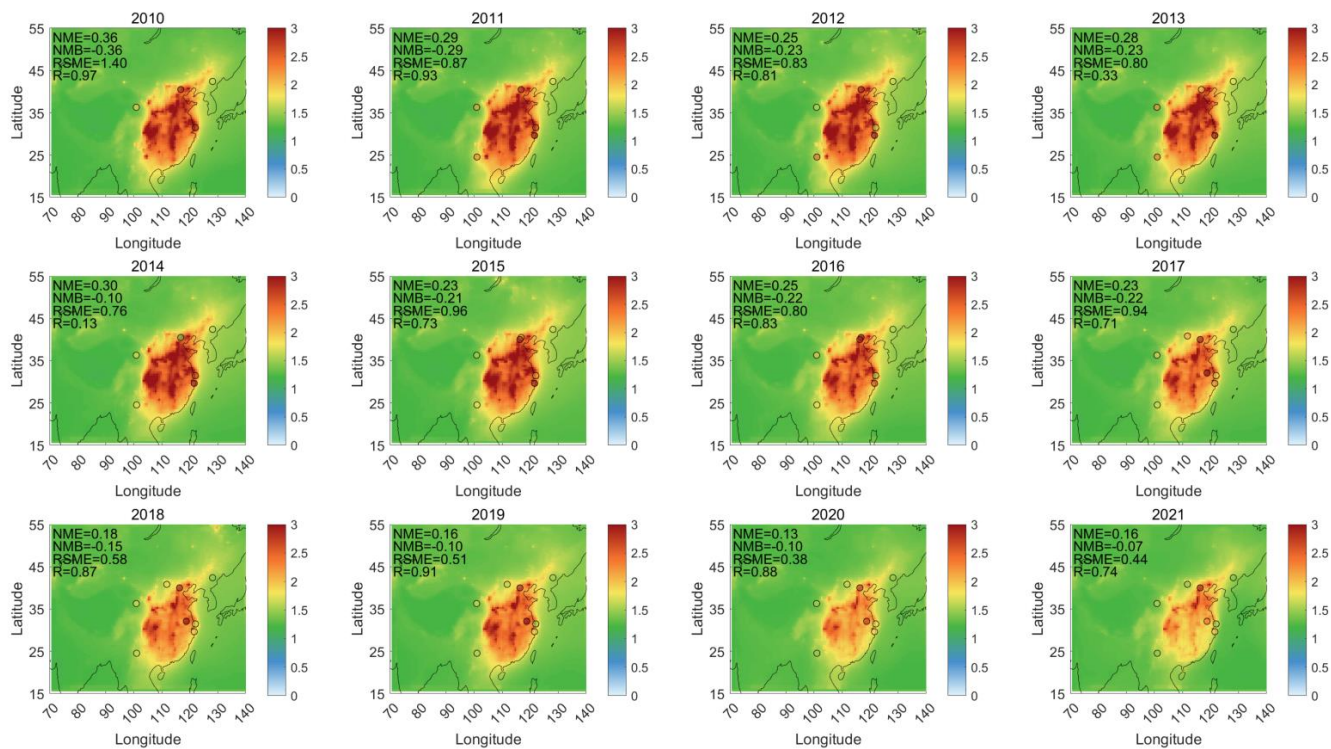


**Figure 5 Temporal and spatial distribution of simulated  $\text{Hg}^0$  concentration ( $\text{ng}/\text{m}^3$ ).**



376

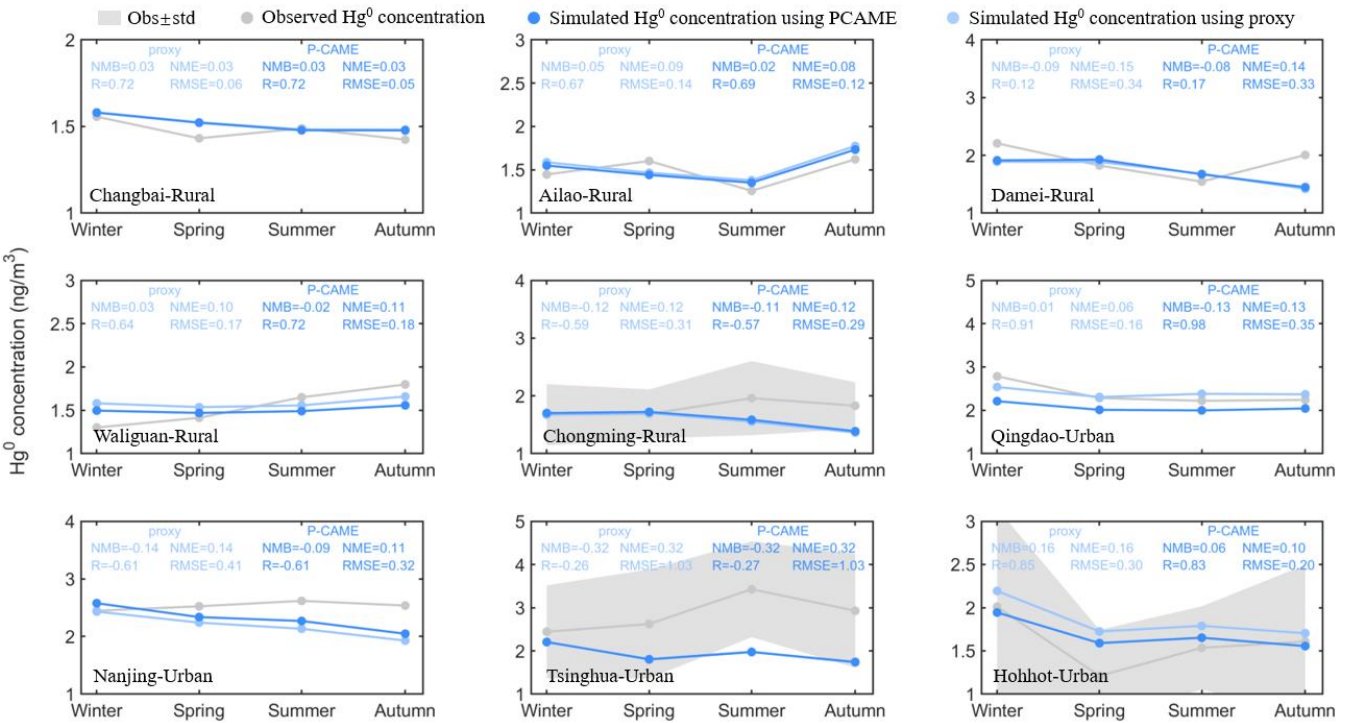
**Table 1 Decline rate of observed Hg<sup>0</sup> concentration, Hg<sup>0</sup> emissions, and simulated Hg<sup>0</sup> concentration**

Sites	Altitude (m a.s.l.)	Type	Period	Decline rate				
				Observed Hg <sup>0</sup> concentration	Simulated Hg <sup>0</sup> concentration	National total Hg <sup>0</sup> emissions	Hg <sup>0</sup> emission of surrounding 9 grids	Hg <sup>0</sup> emission of current grid
Changbai	741	Background	2013-2021	0.22	0.04	0.30	0.58	0.58
Ailao	2450	Background	2012-2021	0.42	0.03	0.35	0.12	0.09
Damie	550	Background	2012-2021	0.46	0.25	0.35	0.38	-0.14
Waliguan	3816	Background	2013-2021	0.29	-0.02	0.30	0.13	-0.12
Chongming	10	Regional Background	2010-2021	0.46	0.21	0.36	0.69	-0.36
Miyun	128	Regional Background	2010-2016	0.31	0.08	0.17	0.42	0.36
Nanjing	10	Urban	2017-2021	0.37	0.19	0.15	0.17	0.35
Tsinghua	50	Urban	2015-2021	0.32	0.06	0.26	0.29	0.38
Hohhot	1100	Urban	2017-2021	0.32	0.05	0.15	0.15	0.04

377 **3.6 Simulation comparison using P-CAME and only proxy-based inventory**

378 We selected 2020 to compare the simulation differences between the P-CAME and only proxy-based inventories, as 2020  
379 exhibits less bias according to Fig. 5. For each site, we compared seasonal average Hg<sup>0</sup> concentrations and evaluated  
380 performance using NMB, NME, RMSE, and R, as detailed in Fig. 6. ~~Comparisons between both simulation scenarios and~~  
381 ~~observations were shown in Fig. 4. For each site, we compared monthly average concentrations and evaluated them using~~  
382 ~~NME and NMB, as shown in Table S4. Our analysis revealed that P-CAME have the potentiality to improve simulation~~  
383 ~~accuracy for urban sites, such as Nanjing and Hohhot. In Nanjing site, the grid containing the Nanjing site includes CFPP and~~  
384 ~~CEM point sources. The only proxy-based method underestimates emissions compared to P-CAME (Fig. S8), resulting in~~  
385 ~~lower simulated Hg<sup>0</sup> concentrations. P-CAME reduces simulation bias, yielding lower NMB, NME, and RMSE values,~~  
386 ~~indicating better agreement with observations. In Hohhot site, the only proxy-based method tends to overestimate emissions~~  
387 ~~due to the high population density (Fig. S8). By contrast, P-CAME produces lower simulated Hg<sup>0</sup> concentrations, which better~~  
388 ~~align with observations, with lower NMB, NME, and RMSE values. These two sites highlight two common scenarios: (1)~~  
389 ~~overestimated emissions in densely populated areas and (2) underestimated emissions in industrial clusters, as discussed in~~  
390 ~~Section 3.1. From this perspective, P-CAME has the capacity to reduce simulation bias by more accurately allocating spatial~~  
391 ~~emissions in urban regions. However, this capacity is currently limited by model bias, such as poor performance in simulating~~  
392 ~~transport processes, as discussed in Section 3.5. For urban sites like Qingdao and Tsinghua, seasonal trends are influenced by~~

air mass sources from different directions, driven by air pressure changes between land and ocean (Shao et al., 2022; Wang et al., 2021). For example, we found that the wind field from MERRA2 does not closely match observations (Fig. S7), which could lead to simulation bias. Since the model struggles to accurately capture these transport processes, its performance at these sites is poor, making it more challenging to identify improvements from revising the emission inventory. The model performs relatively better at rural sites when compared with observations. At these locations, there is little difference in simulation outcomes between using P-CAME and the only proxy-based inventory.



Our findings indicated that P-CAME inventory significantly enhanced GEM simulation in urban areas when compared to non-point source layers. For instance, at the observation site in Hohhot, simulations incorporating point sources resulted in a 23% reduction in both NMB and NME when compared to simulations without point sources (Fig. 4 & Table S4). At the Nanjing site, NMB and NME decreased by 20% and 15%, respectively (Fig. 4 & Table S4). However, the calibration results from the three rural observation stations revealed no significant difference in NMB and NME between simulations with and without point sources (Fig. 4 & Table S4). The improved calibration of urban stations was primarily attributed to the use of point source emissions, which enables more accurate localization of emissions sources. This approach mitigated the issue of overestimation of emissions in urban areas due to high population density in emission allocation using the proxy method.

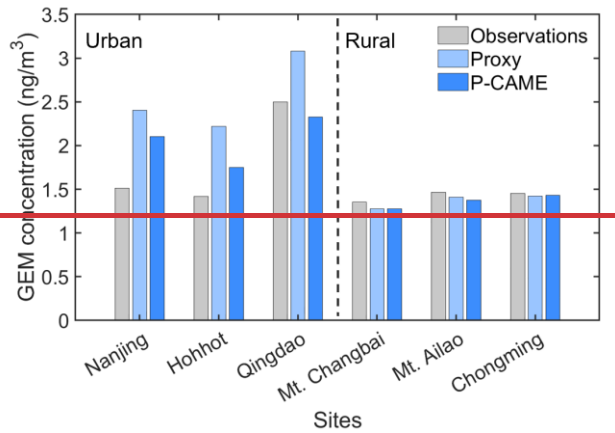


**Figure 64 Comparative analysis** Comparison of observed and simulated atmospheric mercury concentrations using **Proxy-only** proxy-based and P-CAME inventory.

#### 5.4 Data availability

Integrating point source emission inventory (P-CAME) can be accessed from <http://doi.org/10.6084/m9.figshare.26076907> (Cui et al., 2024).

#### 6.5 Conclusions and implications

In this study, we introduce an annual speciated mercury emission inventories (1978-2021), P-CAME inventory. ~~By using this novel inventory, the modelled bias of mercury concentrations in urban sites were significantly reduced, which will significantly improve the understanding of mercury cycling, and thus facilitate the assessment of potential health impacts resulting from exposure to mercury in the environment. Crucially, our inventory's~~ Its accurate, annual, high-resolution emission maps can identify cumulative emission hotspots. The identification of hotspots where cumulative mercury emissions are exceptionally high suggests that targeted pollution control measures could be highly effective. By focusing on these critical areas, which contribute disproportionately to total emissions despite covering a small fraction of the land area, policymakers can allocate resources more efficiently and achieve significant reductions in overall mercury pollution. The substantial presence of  $Hg^{II}$  and  $Hg_P$  in areas dominated by NFMS and CEM points to the potential for severe cross-media mercury pollution. This form of pollution affects not only the air but also water bodies and soils, leading to broader environmental degradation and health risks. Strategies to mitigate mercury emissions areas such as Gansu, Shaanxi, and Hunan Provinces must therefore consider the cross-media implications of mercury pollution.

P-CAME aligns with observed Hg<sup>0</sup> concentration trends over the past decade, showing potential to improve atmospheric mercury simulations, especially in urban areas. However, its effectiveness is limited by the overall model performance. In the future, improvements in spatial accuracy and long-term trend reliability will enhance the inventory's value. These improvements will support more accurate global Hg simulation and deepen our understanding of mercury cycling and the impacts of past emissions. This will be crucial for evaluating the success of the Minamata Convention, helping assess current mercury control policies and guiding future actions to reduce global mercury pollution.

~~By using this novel inventory, the modelled bias of mercury concentrations in urban sites were significantly reduced, which will significantly improve the understanding of mercury cycling, and thus facilitate the assessment of potential health impacts resulting from exposure to mercury in the environment. Crucially, our inventory's~~

~~This publicly accessible inventory, characterized by its temporal and spatial consistency and detailed emission information, provides a critical foundation for nuanced discussions on anthropogenic emissions, atmospheric pollution, and their implications for human health and environmental integrity. The comprehensive nature of the data allows for a deep dive into the sources, distribution, and trends of mercury emissions, facilitating a better understanding of the global mercury cycle and identifying key areas for intervention. Moreover, the inventory's robustness and reliability are instrumental in supporting the initial evaluation of the Minamata Convention's effectiveness. As the first global treaty aimed at protecting human health and the environment from anthropogenic emissions and releases of mercury and mercury compounds, the Convention's success hinges on accurate and comprehensive data. The inventory not only aids in assessing progress towards the Convention's objectives but also highlights areas where further efforts are needed. By providing a solid empirical basis, it enables policymakers, researchers, and environmental advocates to craft more targeted and effective strategies for reducing mercury emissions, ultimately contributing to the global endeavour to mitigate atmospheric pollution and safeguard public health.~~

Owing to constraints in data availability, this study limited its scope to reviewing anthropogenic mercury emissions in China from 1978 onwards, with an incomplete point source coverage. To improve percentage of point sources emissions, future research can incorporate data such as satellite images and visual identity to enhance the accuracy of identification of industrial point sources, thereby refining the inventory of industrial emissions. Additionally, more studies should be conducted across multiple dimensions, including time, space, and emission impacts, potentially incorporating machine learning techniques and AI techniques to expand the temporal and spatial scope of anthropogenic emissions analysis. Those innovative methods could facilitate investigation and assessment of the long-term environmental implications of historical anthropogenic mercury emissions.

455 **Author contributions**

456 Y.C. established the emission inventories and wrote the draft. Q.W. supervised the study, helped conduct data analysis, and  
457 wrote and edited the manuscript. S.W. helped conceive the idea for this article and edited the manuscript. K.L., S.L., Z.S., D.O.,  
458 Z.L. helped to collect and provided basic data for calculation. Q.C. polished the draft. C.L., F.X., Y.T., Y.W. provided ~~GEM~~  
459 Hg<sup>0</sup> concentration data for validation. J.H. helped conceive the idea for this article. All the co-authors revised the manuscript.

460 **Competing interests**

461 The authors declare that they have no conflict of interest.

462 **Disclaimer**

463 Publisher’s note: Copernicus Publications remains neutral with regard to jurisdictional claims in published maps and  
464 institutional affiliations.

465 **Acknowledgements**

466 We express our gratitude to the authors of the articles for providing the observation data utilized in this article. And we extend  
467 our gratitude to numerous staff members at the Environmental Protection Key Laboratory of Sources and Control of Air  
468 Pollution Complex for their invaluable contributions to supplementing the data on point sources.

469 **Financial support**

470 This work was supported by the National Natural Science Foundation of China (No. 2222604, No. 42394094), and National  
471 Key Research and Development Program (No. 2022YFC3700602).

472 **References**

473 Qichacha: <https://www.qcc.com/>, last access: 30 October 2023.  
474 Latitude and longitude query positioning: <http://jingweidu.757dy.com/>, last access: 30 October 2023.  
475 OpenStreetMap: <https://www.openstreetmap.org/>, last access: 30 October 2023.  
476 AMAP/UNEP: AMAP/UNEP geospatially distributed mercury emissions dataset 2010v1 [dataset], 2013.  
477 AMAP/UNEP Technical Background Report to the Global Mercury Assessment 2018, Geneva, Switzerland, 2019.  
478 Amos, H. M., Jacob, D. J., Streets, D. G., and Sunderland, E. M.: Legacy impacts of all-time anthropogenic emissions on the global mercury  
479 cycle, Global Biogeochemical Cycles, 27, 410-421, <https://doi.org/10.1002/gbc.20040>, 2013.

480 Angot, H., Rutkowski, E., Sargent, M., Wofsy, S. C., Hutyra, L. R., Howard, D., Obrist, D., and Selin, N. E.: Atmospheric mercury sources  
481 in a coastal-urban environment: a case study in Boston, Massachusetts, USA, *Environ Sci Process Impacts*, 23, 1914-1929,  
482 10.1039/d1em00253h, 2021.

483 Bishop, K., Shanley, J. B., Riscassi, A., de Wit, H. A., Eklöf, K., Meng, B., Mitchell, C., Osterwalder, S., Schuster, P. F., Webster, J., and  
484 Zhu, W.: Recent advances in understanding and measurement of mercury in the environment: Terrestrial Hg cycling, *Science of The Total*  
485 *Environment*, 721, 137647, <https://doi.org/10.1016/j.scitotenv.2020.137647>, 2020.

486 Brasseur, G. P. and Jacob, D. J.: *Modeling of Atmospheric Chemistry*, Cambridge University Press, Cambridge, DOI:  
487 10.1017/9781316544754, 2017.

488 Chang, J. C. S. and Ghorishi, S. B.: Simulation and Evaluation of Elemental Mercury Concentration Increase in Flue Gas Across a Wet  
489 Scrubber, *Environmental Science & Technology*, 37, 5763-5766, 10.1021/es034352s, 2003.

490 Corbitt, E. S., Jacob, D. J., Holmes, C. D., Streets, D. G., and Sunderland, E. M.: Global Source–Receptor Relationships for Mercury  
491 Deposition Under Present-Day and 2050 Emissions Scenarios, *Environmental Science & Technology*, 45, 10477-10484, 10.1021/es202496y,  
492 2011.

493 Cui, Y., Wu, Q., Wang, S., Liu, K., Li, S., Shi, Z., Ouyang, D., Li, Z., CHen, Q., Lv, C., Xie, F., Tang, Y., Wang, Y., and Hao, J.: Integrating  
494 Point Sources to Map Anthropogenic Atmospheric Mercury Emissions in China, 1978–2021 [dataset], 10.6084/m9.figshare.26076907.v1,  
495 2024.

496 Feinberg, A., Selin, N. E., Braban, C. F., Chang, K. L., Custodio, D., Jaffe, D. A., Kyllonen, K., Landis, M. S., Leeson, S. R., Luke, W.,  
497 Molepo, K. M., Murovec, M., Nerentorp Mastromonaco, M. G., Aspmo Pfaffhuber, K., Rudiger, J., Sheu, G. R., and St Louis, V. L.:  
498 Unexpected anthropogenic emission decreases explain recent atmospheric mercury concentration declines, *Proc Natl Acad Sci U S A*, 121,  
499 e2401950121, 10.1073/pnas.2401950121, 2024.

500 Feng, X., Fu, X., Zhang, H., Wang, X., Jia, L., Zhang, L., Lin, C.-J., Huang, J.-H., Liu, K., and Wang, S.: Combating air pollution  
501 significantly reduced air mercury concentrations in China, *National Science Review*, 11, 10.1093/nsr/nwae264, 2024.

502 Gelaro, R., McCarty, W., Suarez, M. J., Todling, R., Molod, A., Takacs, L., Randles, C., Darmenov, A., Bosilovich, M. G., Reichle, R.,  
503 Wargan, K., Coy, L., Cullather, R., Draper, C., Akella, S., Buchard, V., Conaty, A., da Silva, A., Gu, W., Kim, G. K., Koster, R., Lucchesi,  
504 R., Merkova, D., Nielsen, J. E., Partyka, G., Pawson, S., Putman, W., Rienecker, M., Schubert, S. D., Sienkiewicz, M., and Zhao, B.: The  
505 Modern-Era Retrospective Analysis for Research and Applications, Version 2 (MERRA-2), *J Clim*, Volume 30, 5419-5454, 10.1175/JCLI-  
506 D-16-0758.1, 2017.

507 Giang, A. and Selin, N. E.: Benefits of mercury controls for the United States, *Proceedings of the National Academy of Sciences of the*  
508 *United States of America*, 113, 286-291, 10.1073/pnas.1514395113, 2016.

509 Horowitz, H. M., Jacob, D. J., Zhang, Y., Dibble, T. S., Slemr, F., Amos, H. M., Schmidt, J. A., Corbitt, E. S., Marais, E. A., and Sunderland,  
510 E. M.: A new mechanism for atmospheric mercury redox chemistry: implications for the global mercury budget, *Atmospheric Chemistry*  
511 *and Physics*, 17, 6353-6371, 10.5194/acp-17-6353-2017, 2017.

512 Jung, G., Hedgecock, I. M., and Pirrone, N.: ECHMERIT V1.0 – a new global fully coupled mercury-chemistry and transport model, *Geosci.*  
513 *Model Dev.*, 2, 175-195, 10.5194/gmd-2-175-2009, 2009.

514 Li, Y., Chen, L., Liang, S., Zhou, H., Liu, Y.-R., Zhong, H., and Yang, Z.: Looping Mercury Cycle in Global Environmental–Economic  
515 System Modeling, *Environmental Science & Technology*, 56, 2861-2879, 10.1021/acs.est.1c03936, 2022.

516 Liu, K., Wang, S., Wu, Q., Wang, L., Ma, Q., Zhang, L., Li, G., Tian, H., Duan, L., and Hao, J.: A Highly Resolved Mercury Emission  
517 Inventory of Chinese Coal-Fired Power Plants, *Environmental Science & Technology*, 52, 2400-2408, 10.1021/acs.est.7b06209, 2018.

518 Liu, K., Wu, Q., Wang, L., Wang, S., Liu, T., Ding, D., Tang, Y., Li, G., Tian, H., Duan, L., Wang, X., Fu, X., Feng, X., and Hao, J.:  
519 Measure-Specific Effectiveness of Air Pollution Control on China’s Atmospheric Mercury Concentration and Deposition during 2013–2017,  
520 *Environmental Science & Technology*, 53, 8938-8946, 10.1021/acs.est.9b02428, 2019.

521 Meng, B., Feng, X., Qiu, G., Liang, P., Li, P., Chen, C., and Shang, L.: The process of methylmercury accumulation in rice (*Oryza sativa*  
522 L.), *Environmental Science & Technology*, 45, 2711-2717, 2011.

523 Miao, H., Dong, D., Huang, G., Hu, K., Tian, Q., and Gong, Y.: Evaluation of Northern Hemisphere surface wind speed and wind power  
524 density in multiple reanalysis datasets, *Energy*, 200, 2020.

525 MOHURD (Ministry of Housing and Urban-Rural Development of the People's Republic of China): Interim Provisions on Urban Planning  
526 Quota Index, 1980.

527 Muntean, M., Janssens-Maenhout, G., Song, S., Selin, N. E., Olivier, J. G. J., Guizzardi, D., Maas, R., and Dentener, F.: Trend analysis from  
528 1970 to 2008 and model evaluation of EDGARv4 global gridded anthropogenic mercury emissions, *Science of The Total Environment*, 494-  
529 495, 337-350, <https://doi.org/10.1016/j.scitotenv.2014.06.014>, 2014.

530 Muntean, M., Janssens-Maenhout, G., Song, S., Giang, A., Selin, N. E., Zhong, H., Zhao, Y., Olivier, J. G. J., Guizzardi, D., Crippa, M.,  
531 Schaaf, E., and Dentener, F.: Evaluating EDGARv4.tox2 speciated mercury emissions ex-post scenarios and their impacts on modelled  
532 global and regional wet deposition patterns, *Atmospheric Environment*, 184, 56-68, <https://doi.org/10.1016/j.atmosenv.2018.04.017>, 2018.

533 Omine, N., Romero, C. E., Kikkawa, H., Wu, S., and Eswaran, S.: Study of elemental mercury re-emission in a simulated wet scrubber, *Fuel*,  
534 91, 93-101, <https://doi.org/10.1016/j.fuel.2011.06.018>, 2012.

535 Roy, E. M., Zhou, J., Wania, F., and Obrist, D.: Use of atmospheric concentrations and passive samplers to assess surface-atmosphere  
536 exchange of gaseous mercury in forests, *Chemosphere*, 341, 140113, 10.1016/j.chemosphere.2023.140113, 2023.

537 Selin, N. E.: Global Biogeochemical Cycling of Mercury: A Review, *Annual Review of Environment and Resources*, 34, 43-63,  
538 10.1146/annurev.enviro.051308.084314, 2009.

539 Selin, N. E., Jacob, D. J., Yantosca, R. M., Strode, S., Jaeglé, L., and Sunderland, E. M.: Global 3-D land-ocean-atmosphere model for  
540 mercury: Present-day versus preindustrial cycles and anthropogenic enrichment factors for deposition, *Global Biogeochemical Cycles*, 22,  
541 2008.

542 Shao, L., Wang, Y., Liu, X., Liu, R., Han, K., and Zhang, Y.: Temporal variation of gaseous elemental mercury in a northern coastal city in  
543 China: Monsoon and COVID-19 lockdown effects, *Atmospheric Pollution Research*, 13, 101436, <https://doi.org/10.1016/j.apr.2022.101436>,  
544 2022.

545 Simone, F. D., Gencarelli, C. N., Hedgecock, I. M., and Pirrone, N.: A Modeling Comparison of Mercury Deposition from Current  
546 Anthropogenic Mercury Emission Inventories, *Environmental Science & Technology*, 50, 5154-5162, 10.1021/acs.est.6b00691, 2016.

547 Smith-Downey, N. V., Sunderland, E. M., and Jacob, D. J.: Anthropogenic impacts on global storage and emissions of mercury from  
548 terrestrial soils: Insights from a new global model, *Journal of Geophysical Research*, 115, 10.1029/2009jg001124, 2010.

549 Streets, D. G., Devane, M. K., Lu, Z., Bond, T. C., Sunderland, E. M., and Jacob, D. J.: All-Time Releases of Mercury to the Atmosphere  
550 from Human Activities, *Environmental Science & Technology*, 45, 10485-10491, 10.1021/es202765m, 2011.

551 Streets, D. G., Horowitz, H. M., Lu, Z., Levin, L., Thackray, C. P., and Sunderland, E. M.: Global and regional trends in mercury emissions  
552 and concentrations, 2010-2015, *ATMOSPHERIC ENVIRONMENT*, 201, 417-427, 10.1016/j.atmosenv.2018.12.031, 2019.

553 Sun, P., Song, Z., Qin, Y., Xu, Z., Zhang, Y., Zhong, S., and Yu, J.: Declines of gaseous element mercury concentrations at an urban site in  
554 eastern China caused by reductions of anthropogenic emission, *Atmospheric Environment*, 317, 10.1016/j.atmosenv.2023.120199, 2024.

555 Tang, Y., Wang, S., Wu, Q., Liu, K., Wang, L., Li, S., Gao, W., Zhang, L., Zheng, H., and Li, Z.: Recent decrease trend of atmospheric  
556 mercury concentrations in East China: the influence of anthropogenic emissions, *Atmospheric Chemistry and Physics*, 8279-8291, 2018.

557 Tian, H. Z., Wang, Y., Xue, Z. G., Cheng, K., Qu, Y. P., Chai, F. H., and Hao, J. M.: Trend and characteristics of atmospheric emissions of  
558 Hg, As, and Se from coal combustion in China, 1980–2007, *Atmos. Chem. Phys.*, 10, 11905-11919, 10.5194/acp-10-11905-2010, 2010.

559 Tian, H. Z., Zhu, C. Y., Gao, J. J., Cheng, K., Hao, J. M., Wang, K., Hua, S. B., Wang, Y., and Zhou, J. R.: Quantitative assessment of  
560 atmospheric emissions of toxic heavy metals from anthropogenic sources in China: historical trend, spatial distribution, uncertainties, and  
561 control policies, *Atmos. Chem. Phys.*, 15, 10127-10147, 10.5194/acp-15-10127-2015, 2015.

562 van der Werf, G. R., Randerson, J. T., Giglio, L., van Leeuwen, T. T., Chen, Y., Rogers, B. M., Mu, M., van Marle, M. J. E., Morton, D. C.,  
563 Collatz, G. J., Yokelson, R. J., and Kasibhatla, P. S.: Global fire emissions estimates during 1997–2016, *Earth System Science Data*, 9, 697-  
564 720, 10.5194/essd-9-697-2017, 2017.

565 Wang, C., Wang, Z., and Zhang, X.: Speciated atmospheric mercury during haze and non-haze periods in winter at an urban site in Beijing,  
566 China: Pollution characteristics, sources, and causes analyses, *Atmospheric Research*, 247, 10.1016/j.atmosres.2020.105209, 2021.

567 Wu, Q., Wang, S., Li, G., Liang, S., Lin, C.-J., Wang, Y., Cai, S., Liu, K., and Hao, J.: Temporal Trend and Spatial Distribution of Speciated  
568 Atmospheric Mercury Emissions in China During 1978–2014, *Environmental Science & Technology*, 50, 13428-13435,  
569 10.1021/acs.est.6b04308, 2016.



570 Wu, Q. R., Wang, S. X., Zhang, L., Song, J. X., Yang, H., and Meng, Y.: Update of mercury emissions from China's primary zinc, lead and  
571 copper smelters, 2000&ndash;2010, *Atmos. Chem. Phys.*, 12, 11153-11163, 10.5194/acp-12-11153-2012, 2012.

572 Wu, X., Fu, X., Zhang, H., Tang, K., Wang, X., Zhang, H., Deng, Q., Zhang, L., Liu, K., Wu, Q., Wang, S., and Feng, X.: Changes in  
573 Atmospheric Gaseous Elemental Mercury Concentrations and Isotopic Compositions at Mt. Changbai During 2015–2021 and Mt. Ailao  
574 During 2017–2021 in China, *Journal of Geophysical Research: Atmospheres*, 128, e2022JD037749, <https://doi.org/10.1029/2022JD037749>,  
575 2023.

576 Wu, Y., Wang, S., Streets, D. G., Hao, J., Chan, M., and Jiang, J.: Trends in Anthropogenic Mercury Emissions in China from 1995 to 2003,  
577 *Environmental Science & Technology*, 40, 5312-5318, 10.1021/es060406x, 2006.

578 Xu, X.: China population spatial distribution kilometer grid dataset. Resource and environmental science data registration and publication  
579 system (<http://www.resdc.cn/DOI>) [dataset], 10.12078/2017121101, 2017.

580 Yang, L. H., Jacob, D. J., Dang, R., Oak, Y. J., Lin, H., Kim, J., Zhai, S., Colombi, N. K., Pendergrass, D. C., Beaudry, E., Shah, V., Feng,  
581 X., Yantosca, R. M., Chong, H., Park, J., Lee, H., Lee, W.-J., Kim, S., Kim, E., Travis, K. R., Crawford, J. H., and Liao, H.: Interpreting  
582 Geostationary Environment Monitoring Spectrometer (GEMS) geostationary satellite observations of the diurnal variation in nitrogen  
583 dioxide (NO<sub>2</sub>) over East Asia, *Atmospheric Chemistry and Physics*, 24, 7027-7039, 10.5194/acp-24-7027-2024, 2024.

584 Zhang, L.: Emission characteristics and synergistic control strategies of atmospheric mercury from coal combustion in China, School of  
585 Environment, Tsinghua University, Beijing, 2012.

586 Zhang, L., Wang, S., Meng, Y., and Hao, J.: Influence of Mercury and Chlorine Content of Coal on Mercury Emissions from Coal-Fired  
587 Power Plants in China, *Environmental Science & Technology*, 46, 6385-6392, 10.1021/es300286n, 2012.

588 Zhang, L., Wang, S., Wu, Q., Wang, F., Lin, C. J., Zhang, L., Hui, M., Yang, M., Su, H., and Hao, J.: Mercury transformation and speciation  
589 in flue gases from anthropogenic emission sources: a critical review, *Atmos. Chem. Phys.*, 16, 2417-2433, 10.5194/acp-16-2417-2016, 2016a.

590 Zhang, L., Wang, S., Wang, L., Wu, Y., Duan, L., Wu, Q., Wang, F., Yang, M., Yang, H., Hao, J., and Liu, X.: Updated Emission Inventories  
591 for Speciated Atmospheric Mercury from Anthropogenic Sources in China, *Environmental Science & Technology*, 49, 3185-3194,  
592 10.1021/es504840m, 2015.

593 Zhang, Y., Zhang, L., Cao, S., Liu, X., Jin, J., and Zhao, Y.: Improved Anthropogenic Mercury Emission Inventories for China from 1980  
594 to 2020: Toward More Accurate Effectiveness Evaluation for the Minamata Convention, *Environmental Science & Technology*, 57, 8660-  
595 8670, 10.1021/acs.est.3c01065, 2023.

596 Zhang, Y., Jacob, D. J., Horowitz, H. M., Chen, L., Amos, H. M., Krabbenhoft, D. P., Slemr, F., St. Louis, V. L., and Sunderland, E. M.:  
597 Observed decrease in atmospheric mercury explained by global decline in anthropogenic emissions, *Proceedings of the National Academy  
598 of Sciences*, 113, 526-531, 10.1073/pnas.1516312113, 2016b.

599 Zhao, Y., Zhong, H., Zhang, J., and Nielsen, C. P.: Evaluating the effects of China's pollution controls on inter-annual trends and uncertainties  
600 of atmospheric mercury emissions, *Atmos. Chem. Phys.*, 15, 4317-4337, 10.5194/acp-15-4317-2015, 2015.

601